JOURNAL OF AIRCRAFT
Vol. 46, No. 6, November–December 2009

Dynamic Response of a High-Altitude Tethered Balloon System

G. S. Aglietti*
University of Southampton, Southampton, England SO17 1BJ, United Kingdom

DOI: 10.2514/1.43332

This paper illustrates a procedure to calculate the response of a tethered spherical aerostat to gusts, including the effect of structural nonlinearity and accounting for some of the fluid–structure interaction between the aerostat and tether line. The procedure developed and presented here is based on a full three-dimensional dynamic finite element model, with aerodynamic loads calculated from the relative velocity between a time-varying input airflow and resulting structural velocities. Exact solutions for the static response and a simplified dynamic model, both developed to validate the results of the procedure illustrated in this paper, are also derived and described in detail. The dynamic responses to gusts are compared with the equivalent steady-state solution to assess the approximations of the static solutions. Particular emphasis is placed on the output rotation of the aerostats to quantify disturbances on the pointing stability produced by gusts.

Nomenclature

B	=	aerostat buoyancy
C_{DS}	=	drag coefficient of a sphere
$C_{D\alpha}$	=	drag coefficient
C_{D0}	=	drag coefficient for a cylinder perpendicular to the incoming airflow
$C_{L\alpha}$	=	lift coefficient
$\mathbf{D}_n$	=	drag force vector for node n
$\mathrm{d}s$	=	infinitesimal length of tether
$\mathbf{e}_n$	=	vector representing nth element
$\mathbf{F}_t$	=	aerodynamic force matrix (forces on the nodes of the tether)
$\mathbf{f}_A$	=	aerostat aerodynamic force vector
$\mathbf{f}_n$	=	aerodynamic force vector for node n
$\mathbf{L}_n$	=	lift force vector for node n
M_{aero}	=	mass of the aerostat
m_t	=	mass of the tether
N	=	total number of nodes
n	=	node number index
p	=	drag force per unit length along the tether line
Re	=	Reynolds number
S	=	total length of the tether
T_H	=	horizontal force along the tether line
T_V	=	vertical force along the tether line
T_0	=	reference temperature for air density calculations (troposphere −56.5°C)
$\mathbf{v}^r$	=	relative wind velocity vector
$\mathbf{v}^w$	=	absolute wind velocity vector
w	=	weight per unit length of the tether line
w_t	=	total vertical force per unit length along the tether line
x	=	x coordinate
y	=	y coordinate
z	=	z coordinate
α	=	angle between the tether element and wind velocity vector
θ	=	angle of small oscillation of the tether
ρ_n	=	air density at node n
ρ_0	=	air density at sea level
ϕ_A	=	aerostat diameter
ϕ_T	=	tether cable diameter

Received 20 January 2009; revision received 26 July 2009; accepted for publication 27 July 2009.

*Reader, School of Engineering Sciences, Highfield. Member AIAA.

I. Introduction

IN THE last few years, aerostats have attracted renewed interest, which has been a welcome development in the lighter-than-air research and development community. This surge of research interest has its roots in advances made in the materials typically used for the aerostats' envelopes, which has led to an improvement in performance. This, in turn, has produced an expansion of the typical market niches of these devices [scientific ballooning, surveillance/reconnaissance (see, for example, [1]) and the U.S. Air Force data sheet [2]], with more researchers proposing different applications, ranging from high-altitude aerostats as astronomical platforms [3] to infrastructures for communication systems [4].

Tethered aerostats are limited to lower altitudes due to the weight of the tether, which increases linearly with length. Currently, tethered aerostats can fly up to approximately 8 km [3], but various studies have been conducted to prove that considerably greater altitudes can be reached. For example, the Johns Hopkins University Applied Physics Laboratory has conducted a feasibility study (although not experimentally demonstrated) on a high-altitude (20 km) tethered-balloon-based space-to-ground optical communication system [4]. The U.S. Air Force has made extensive use of tethered aerostats as surveillance systems, and there are available on the market aerostats such as the Puma tethered aerostat or TCOM's 71M, which can fly up and beyond 5 km altitude tethered with a cable that supplies the aerostat onboard systems with electric power. These aerostats are designed for long-duration missions and they are designed to be able to withstand lightning strikes and strong winds.

Weather survival is one of the major challenges in aerostat design, particularly for moored craft intended for long-duration operations, and the evaluation of their dynamic response is a crucial step in the design.

Most of the work in this area deals with streamlined aerostats. In [5], for example, an aerostat response to simulated turbulence is considered, using a nonlinear 2-D model of the system, and focusing on the development of an appropriate aerodynamic loading derived from real hurricane data. In [6] a streamlined aerostat is considered, and in [7] the theoretical predictions are correlated with real data from full-scale flight tests of a TCOM 71M tethered aerostat. In fact, in general, streamlined aerostats generate less drag force compared with spherical aerostats, and this is a considerable advantage for the tether system, especially in strong winds. In addition, their weathervaning behavior gives a certain degree of stability to the system, which, again, can be advantageous for some applications.

However, mainly due to their inherent simplicity, spherical aerostats are still an appropriate choice for several applications and there have been studies to evaluate their design (see, for example, [8]) and their response to severe weather conditions [9]. Although it is acknowledged that spherical aerostats are less stable than streamlined aerostats, there are still applications such as [10] that require an assessment of their three-dimensional pointing stability.

This paper extends the work in [9], which presents a 2-D analysis of a high-altitude balloon tethered using a lump mass and spring model for the cable, by considering a 3-D case that also includes the cable bending stiffness. To include the bending stiffness is particularly relevant for large cables containing substantial electrical conductors, insulators, and lightning protection, which can have a nonnegligible bending stiffness. Three-dimensional models of tether line dynamics are indeed available, in particular, for marine mooring lines [11–13]. However, in these applications they are coupled with the dynamics of a floating vessel, which is substantially different from that of a tethered sphere.

There is also a substantial amount of literature available on sphere aerodynamics (see, for example, the early work in [14] and more recently [15–17], just to quote a few examples), and more specific to the case of tethered spheres is the considerable body of research work on their vortex-induced vibrations (see, for example, [18–21]). However, in all these models, the fluid loading on the tether line and its mass are neglected. For applications in which the tether is a substantial cable (e.g., [6,10]), the loading on the tether and its mass are of similar magnitude to those of the balloon, and therefore their influence cannot be neglected. In addition, the published work on tethered spheres does not cover the supercritical region of the Reynolds number, which is relevant for large tethered aerostats in strong winds.

Finally, there is also a considerable amount of published work on cable dynamics (see, for example, [22,23]), which is itself an extremely complicated fluid–structure interaction problem.

Because of their interaction, the dynamic behavior of cable and balloon cannot be modeled separately. However, to model the response of a tethered balloon at supercritical Reynolds number, including the dynamics of the cable, the integration of the aforementioned state-of-the-art research work on vortex-induced vibrations into a single mathematical model is undoubtedly an overwhelming task. In addition, such a complex mathematical model might be impractical to use in an industrial environment, particularly during the preliminary design phase, in which the designer is often trying to assess a realistic worst-case scenario using practical tools such as the finite element method.

As an alternative, what is proposed here is the possibility to simulate the overall system dynamics using standard finite element software imbedded in an algorithm that considers the fluid–structure interaction. This procedure is demonstrated here using a relatively simple fluid dynamic model based on standard expressions for the aerodynamic loading, depending on the relative angle and velocity between the airflow and the structure. Standard test cases (i.e., a gust superimposed to a constant wind) are considered for the airflow. However, any type of 3-D space- and time-varying wind field could be used as input.

II. Mathematical Model

The mathematical model that describes the system is relatively simple. The structure (i.e., tether and balloon) is modeled using commercial finite element (FE) software (ANSYS). The tether model is initially built by meshing a straight line with N beam elements and the aerostat is represented by a point mass of appropriate inertia connected to the last node ($N + 1$) along the line. The use of beam elements that use a combination of first- and second-order shape functions and distributed mass, instead of lumped masses connected by springs (as in [9]), allows the inclusion of the cable bending stiffness that in some cases could be nonnegligible. Appropriate density is applied to the elements to reproduce the weight of the cable.

The first node of the line is grounded to represent the mooring station.

The node representing the aerostat is loaded with a vertical force, the aerostat buoyancy, plus a force vector $\mathbf{f_A}$ that reproduces the x, y, and z components of the aerodynamic loads on the aerostat.

The nodes along the tether line are subjected to a load matrix $\mathbf{F_t}$ (size of the matrix $N - 1 \times 3$), where each row contains the x, y, and z components of the aerodynamic forces on the cable segment close to that node.

Gravity acceleration is also included as a load in the FE model to reproduce the forces produced by the weight of the elements.

The numerical solution is carried out in the time domain, and at each time step of the solution process, the force vector $\mathbf{f_A}$ and the matrix $\mathbf{F_t}$ are updated to reproduce the effect of changes in the external loads (e.g., to represent a gusts profile summed to a constant wind speed) and to include the effect of the interaction between the dynamics of the structure and the surrounding airflow.

Clearly, the selection of an appropriate time step is crucial to the accuracy of the solution, as this must be able to give a smooth representation of the input transients and, most important, must be able to resolve the frequency content of the dynamic response of the structure.

In practice, the core of the solution process is the FE code that implements a transient nonlinear analysis (including stress stiffening). The FE solver is imbedded in a loop that is executed at each time step and that updates the input for the next solution, taking into account the changes in the external loads (i.e., wind speed and direction) and subtracting the velocity of the structural response, as the applied aerodynamic forces ultimately depend on the relative velocity vector between airflow and structure. This procedure represents the aerodynamic damping well, provided that accurate coefficients are used in the equations that deliver the aerodynamic forces.

To be able to implement the procedure described previously, the aerodynamic forces that populate the matrix $\mathbf{F_t}$ and the vector $\mathbf{f_A}$ must be calculated. For the moment, the unsteady aerodynamics that produce vortices and fluctuation of the aerodynamic loads are neglected and the aerodynamic forces are directly calculated from the relative velocity $\mathbf{v}^r$ between the local wind velocity vector $\mathbf{v}^\mathbf{w}$ and the velocity of the structure (calculated as the time derivative of the nodal displacements $\mathbf{x}$):

$$\mathbf{v}_n^r(t) = \mathbf{v}_n^w - \dot{\mathbf{x}}_n \tag{1}$$

where (t) denotes time dependence and the subscript n has been introduced to indicate the value at the particular node. Note that any type of 3-D space- and time-varying wind field can be used as input, provided that it can be put into a time-varying matrix in which each of the N rows defines the three components (x y, and z) of wind speed at the nth node location.

The tether is essentially a cylinder inclined to the approaching flow, and although the loads applied may produce relatively large displacements and curvatures (such that the cable's overall shape deviates significantly from that of the ideal straight cylinder), the curvature is still significantly smaller that the elements' lengths or their cross sections (see Fig. 1). Therefore, the elements that make up the tether can be considered straight cylinders with varying inclinations with respect to the approaching flow, and aerodynamic forces can be calculated starting from the 2-D lift and drag coefficients derived in the ESDU International data sheet [24]. These coefficients, rearranged to follow the reference system sketched in Fig. 1, become

$$C_{D\alpha} = C_{D0}\left(\sin^3\alpha + 0.033\left(\frac{\pi}{2} - \alpha\right)\left(\frac{4-\pi}{2} - \alpha\right)\cos\alpha\right) \tag{2}$$

$$C_{L\alpha} = C_{D0}\left(-\sin^2\alpha\cos\alpha + 0.033\left(\frac{\pi}{2} - \alpha\right)\left(\frac{4-\pi}{2} - \alpha\right)\sin\alpha\right) \tag{3}$$

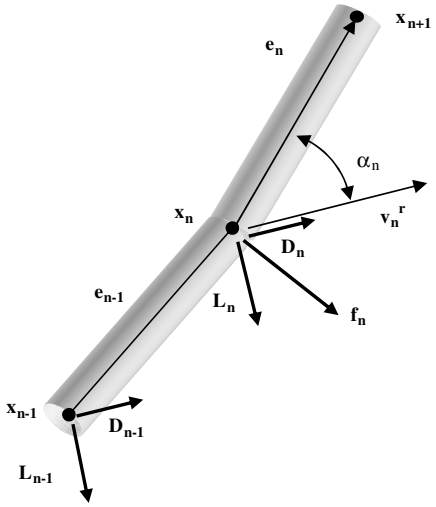

Fig. 1 Tether elements and wind vector.

where C_{D0} is the drag coefficient for a cylinder perpendicular to the direction of the airflow, and α is the angle between the element axis and the wind vector.

Taking that the nth element can be defined by the vector

$$\mathbf{e}_n = \mathbf{x}_{n+1} - \mathbf{x}_n \tag{4}$$

where $\mathbf{x_{n+1}}$ and $\mathbf{x_n}$ are the positions of its connecting nodes, it follows that

$$\frac{\mathbf{v}_n^r \cdot \mathbf{e}_n}{|\mathbf{v}_n^r||\mathbf{e}_n|} = \cos\alpha_n \tag{5}$$

where α_n is the angle between the relative wind velocity (at the node n) and the longitudinal direction of the nth element of the tether.

Therefore, it is possible to calculate the aerodynamic lift vector (perpendicular to the local wind vector and lying on the plane identified by this vector and the tether element) and the drag vector (parallel to the relative wind velocity vector):

$$\mathbf{D}_n = \frac{1}{2}\rho_n \mathbf{v}_n^r C_{D0}\phi_T\left(|\mathbf{v}_n^r \times \mathbf{e}_n|\left(1 - \left(\frac{\mathbf{v}_n^r \cdot \mathbf{e}_n}{|\mathbf{v}_n^r||\mathbf{e}_n|}\right)^2\right) + 0.033\alpha_n(2-\alpha_n)\frac{\mathbf{v}_n^r \cdot \mathbf{e}_n}{|\mathbf{v}_n^r||\mathbf{e}_n|}\right) \tag{6}$$

$$\mathbf{L}_n = \frac{1}{2}\rho_n C_{D0}\phi_T \mathbf{v}_n^r \times \mathbf{v}_n^r \times \mathbf{e}_n\left(\frac{\mathbf{v}_n^r \cdot \mathbf{e}_n}{|\mathbf{v}_n^r||\mathbf{e}_n|}\sqrt{1 - \left(\frac{\mathbf{v}_n^r \cdot \mathbf{e}_n}{|\mathbf{v}_n^r||\mathbf{e}_n|}\right)^2} - 0.033\alpha_n(2-\alpha_n)\right) \tag{7}$$

where ρ_n represents the air density at the altitude of the node n, calculated using Eq. (8), which gives a good approximation of the standard atmosphere in the range of altitudes considered in this work, and ϕ_T is the tether diameter. In Eq. (8) ρ_0 indicates the air density at sea level, z is the altitude of the specific node expressed in meters, and T_0 is a reference temperature that is equal to −56.5°C:

$$\rho(z) = \rho_0\left(\frac{T_0 - 0.0065z}{T_0}\right)^{4.2561} \tag{8}$$

With reference to Eqs. (6) and (7), the last term that appears in both equations is relatively small compared with the other term and therefore can be neglected without significant loss of accuracy.

Although C_{D0} is a function of Reynolds number, for this application (with wind velocities between 0.5 and 50 m/s), this ranges from 10^3–10^5, and within this range C_{D0} can be assumed constant and equal to 1. However, more precise expressions can be used to describe C_{D0} as a function of Reynolds number, and the cable roughness can also be considered in the calculation, as illustrated in the ESDU International data sheet [24].

Drag and lift are evaluated for both elements connected to each node of the tether and the actual force applied at that node is the sum of the vectors averaged between the two elements so that each row of the matrix $\mathbf{F_t}$ is equal to

$$\mathbf{f}_n = \frac{\mathbf{L_n} + \mathbf{L_{n-1}}}{2} + \frac{\mathbf{D_n} + \mathbf{D_{n-1}}}{2} \tag{9}$$

Concerning the aerostat, the wind velocities considered here produce a supercritical regime with Reynolds numbers ranging from 10^6 to 10^8 and a drag coefficient C_{DS} approximately equal to 0.2 (see, for example, [16]). Therefore, neglecting for the moment the lateral force produced by the asymmetric shedding of vortices and unsteady aerodynamic phenomena, the force on the aerostat can be calculated using the following expression:

$$\mathbf{D}_N = \frac{1}{2}\rho_N|\mathbf{v}_N^r|\mathbf{v}_N^r C_{DS}\pi\left(\frac{\phi_A}{4}\right)^2 \tag{10}$$

where ϕ_A is the tethered balloon diameter.

The process described previously is summarized in the flowchart in Fig. 2.

It is acknowledged that, in reality, the aerodynamic loads are considerably more complex than the steady-state aerodynamic loads expressed by Eqs. (6) and (7) or Eq. (10), as vortex-induced vibrations induce lateral forces and fluctuations of these loads. However, these equations or their equivalents are still the most practical tools used during the preliminary design. More detailed expressions of the aerodynamic loads as time-varying functions of the angle of attack and relative velocity can be substituted in Eqs. (6) and (7) or Eq. (10) if they are available.

III. Model Implementation and Validation

In addition to standard FE model checks, the model and solution processes described previously were validated against theoretical results. Two separate validations were carried out: the first one to verify the quasi-static response of the system and the second to verify the dynamics. This validation philosophy is implemented in practice by considering a specific design (i.e., fixing the design variables such as aerostat size, altitude, etc.) for which the response is then calculated using the procedure described previously and using an analytical approach.

For the static tests, the input is a constant wind speed and the program is left to converge to the appropriate deformed shape. For the dynamic tests, a gust is used to excite the system, producing

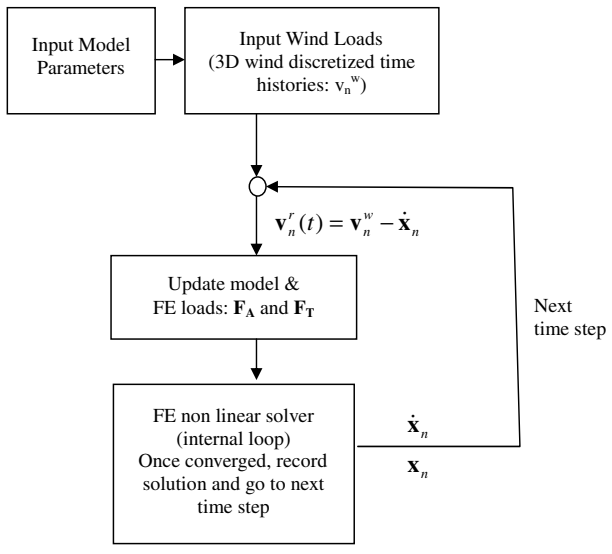

Fig. 2 Solution scheme summary flowchart.

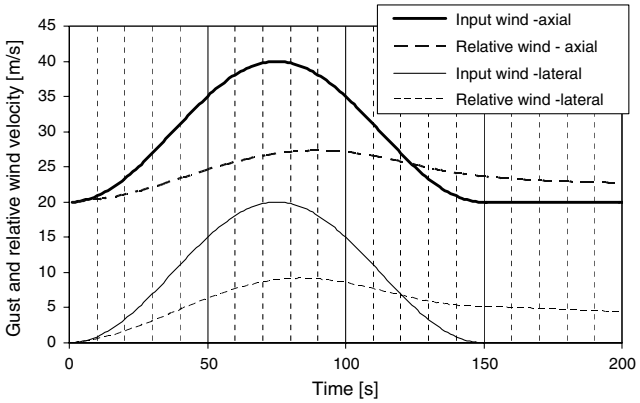

Fig. 3 Wind profile and relative wind velocity in the direction of the gust.

oscillations that are then compared with a simplified theoretical solution.

In practice, a gust velocity vector with 1 cos magnitude and duration, discussed in the next section (see Fig. 3), is summed to the constant wind speed, and the time response of the system is compared with theoretical results.

The specific design that is considered here is that described in detail in [10] and the main parameters are reported in Table 1. Basically, the specific values of these parameters are calculated from the typical data for aerostats of various size, which are reported in [25]. Using the volume of the aerostat as independent variable and interpolating between the data points (that represent the characteristics of existing aerostats), it is possible to derive the weight of the various subsystems (e.g., envelope, ballonet, reinforcements/structural components, etc.), which yield a total mass of the aerostat of approximately 12,000 kg. Concerning the cable, this is used to mechanically secure the aerostat to the ground and to transport electric energy between the aerostat and ground. Hence, the mechanical properties are calculated considering a load bearing part of aramid fibers (from Dupont Kevlar 49 with strength up to 3.62 GPa and densities of 1.45 kg/m^3) and aluminum conductors. In fact, although copper has a higher conductivity than aluminum, its specific mass is considerably higher; therefore, aluminum is chosen for all the applications in which high conductivity over mass is required (e.g., overhead power lines). The resulting properties are reported in Table 1.

A. Quasi-Static Verification

The first step was the validation of the deformed shape of the tether, subjected to the forces produced by the aerostat applied at one end and the distributed loads due to the aerodynamic forces and the tether's own weight applied along the cable length. This required an extension of the standard catenary equations, to include the horizontal loads and the stretching of the cable. Assuming a wind field with constant direction, the problem can be reduced from three to two dimensions (as the sagging cable lies on the plane identified by the wind vector and local gravity force vector).

Table 1 Design parameters

Parameter	Description	Assumed value
B	Aerostat buoyancy at 7500 m	54×10^4 N
R	Aerostat radius	30 m
Vol	Aerostat volume	113×10^3 m^3
W_{aerosta}	Mass of the aerostat (including subsystems and PV cells)	12×10^3 kg
S_T	Length of the tether	7500 m
W_T	Mass of the tether	28×10^3 kg
EA_T	Axial stiffness of the tether	8.57×10^7 N
N	Number of elements in the tether line	500

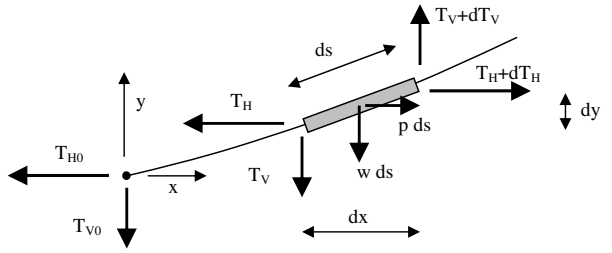

Fig. 4 Forces acting at the grounding point and on an infinitesimal segment of the tether.

With reference to Fig. 4, T_H and T_V are the horizontal and vertical components of the force on the tether, respectively; p is the drag force per unit length produced by the wind; and w_t is the vertical force per unit length that is the sum of the weight and lift per unit length of the tether:

$$p = \tfrac{1}{2}\rho_{\text{air}} v^2 C_{D\alpha} \phi_T \tag{11}$$

$$w_t = w + \tfrac{1}{2}\rho_{\text{air}} v^2 C_{L\alpha} \phi_T \tag{12}$$

where $C_{D\alpha}$ and $C_{L\alpha}$ can be calculated using Eqs. (2) and (3). Following the procedure described in the Appendix, the vertical and horizontal displacements of the tether can be written as

$$\begin{aligned} y = &\left(\frac{T_{V0}}{q} - \frac{2w(T_{V0}w_t - T_{H0}p)}{2q^2}\right) \\ &\times \left(\operatorname{asinh}\left(\frac{w_t^2 s + (T_{V0}w_t - T_{H0}p)}{\sqrt{q^2T_0^2 - (T_{V0}w_t - T_{H0}p)^2}}\right)\right. \\ &\left. - \operatorname{asinh}\left(\frac{(T_{V0}w_t - T_{H0}p)}{\sqrt{q^2T_0^2 - (T_{V0}w_t - T_{H0}p)^2}}\right)\right) \\ &+ + \frac{w(\sqrt{(T_{H0} - ps)^2 + (T_{V0} + w_t s)^2} - T_0)}{q^2} \\ &+ \frac{T_{V0}s}{\frac{EA}{L}} + \frac{w_t s^2}{2\frac{EA}{L}} \end{aligned} \tag{13}$$

and

$$\begin{aligned} x = &\left(\frac{T_{H0}}{q} + \frac{2p(T_{V0}w_t - T_{H0}p)}{2q^3}\right) \\ &\times \left(\operatorname{asinh}\left(\frac{q^2 s + (T_{V0}w_t - T_{H0}p)}{\sqrt{q^2T_0^2 - (T_{V0}w_t - T_{H0}p)^2}}\right)\right. \\ &\left. - \operatorname{asinh}\left(\frac{(T_{V0}w_t - T_{H0}p)}{\sqrt{q^2T_0^2 - (T_{V0}w_t - T_{H0}p)^2}}\right)\right) \\ &+ - \frac{p(\sqrt{(T_{H0} - ps)^2 + (T_{V0} + w_t s)^2} - T_0)}{q^2} \\ &+ \frac{T_{H0}s}{\frac{EA}{L}} + \frac{ps^2}{2\frac{EA}{L}} \end{aligned} \tag{14}$$

To obtain the closed-form solution expressed by the preceding equations, p and w_t have to be assumed as constant along the tether line.

The comparison between the results obtained using the FE-based procedure and those obtained using the theory developed in the Appendix and captured in Eqs. (13) and (14) is plotted in Fig. 5. For both cases considered (i.e., 20 and 40 m/s wind), the deformed shapes of the cable are in excellent agreement. It must be noted that the procedure to obtain the closed-form theoretical solution assumes constant loadings p and w_t along the line; therefore, in the comparison, these have been considered constant. The value for the air density that appears in (11) and (12) is taken as the average between ground level and the balloon altitude, and the angle of the tether line that appears in the lift and drag coefficient is taken as the angle

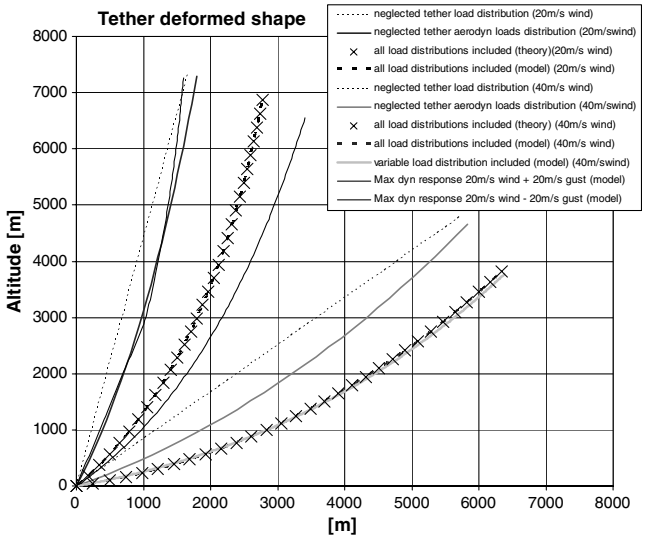

Fig. 5 Tether deformed shape for various approximations.

between a straight line that connects the aerostat with the mooring point and the wind direction. The FE-based procedure starts with the tether line in the vertical position and runs until convergence is achieved for the solution shown in Fig. 5. The average densities achieved at convergence of the FE solution and angle of attack are then used to calculate the average (constant) values for p and w_t, and the parameters in Eqs. (13) and (14) are calculated using the values in Table 1. The excellent match of the curves in Fig. 5 shows that the FE-based model does indeed converge to the theoretical solution. However, the FE-based solution allows for variation of the loading along the line (due, for example, to the variation of air density with altitude) or variation of the angle of the cable (due to its sagging) or a variable wind profile. The impact of variations of density and angle of attack can also be seen in Fig. 5 for the 40 m/s wind case.

B. Dynamic Response Verification

A simple check on the capability of the model to correctly reproduce the overall dynamics of the system can be made by comparing the period of the oscillations around a position of equilibrium with that of an inverted pendulum with equivalent characteristics.

With reference to Fig. 6, and under the assumption that the tether is a straight line, the equation governing small oscillations about the position of equilibrium is

$$\left(M_{\text{aero}}S^2 + \frac{m_t S^2}{3}\right)\ddot{\theta} = -\sqrt{\left(B - M_{\text{aero}}g - \frac{w_t S}{2}\right)^2 + \left(D + \frac{pS}{2}\right)^2}\, S \sin\theta \tag{15}$$

where θ represents the rotation of the system; M_{aero} and m_t are the mass of the aerostat and tether, respectively; and B is the aerostat buoyancy. Also assuming slow oscillations allows one to consider the aerodynamic forces in (15) as constants; hence, neglecting the damping yields a simple harmonic response solution that will have a period

$$T = 2\pi\sqrt{\frac{(M_{\text{aero}}S^2 + (m_t S^2/3))}{\sqrt{(B - M_{\text{aero}}g - (w_t S/2))^2 + (D + (pS/2))^2}\, S}} \tag{16}$$

Regarding the real system implemented in the algorithm described in Sec. II, its damping is mainly produced by the fluctuations of the aerodynamic forces (opposite to the motion) and is proportional to the square of the relative velocity between the wind and structural velocity response [Eq. (1)]. When there is no wind, the damping force is simply proportional to the square of the structural velocity and is in the opposite direction. In this case, for relatively small and slow oscillations, the damping force is quite small and the system exhibits an underdamped behavior for which the period can be legitimately compared with Eq. (16). However, when wind is present, the square of the relative velocity between structure and surrounding airflow can become substantial even for small oscillations, and the aerodynamic drag opposite to the motion can produce an overdamped behavior. In this case, the easiest option to allow the comparison between the model and the benchmark [i.e., Eq. (16)] is to set the damping force to zero in the model to obtain oscillations for which the period can then be compared with Eq. (16).

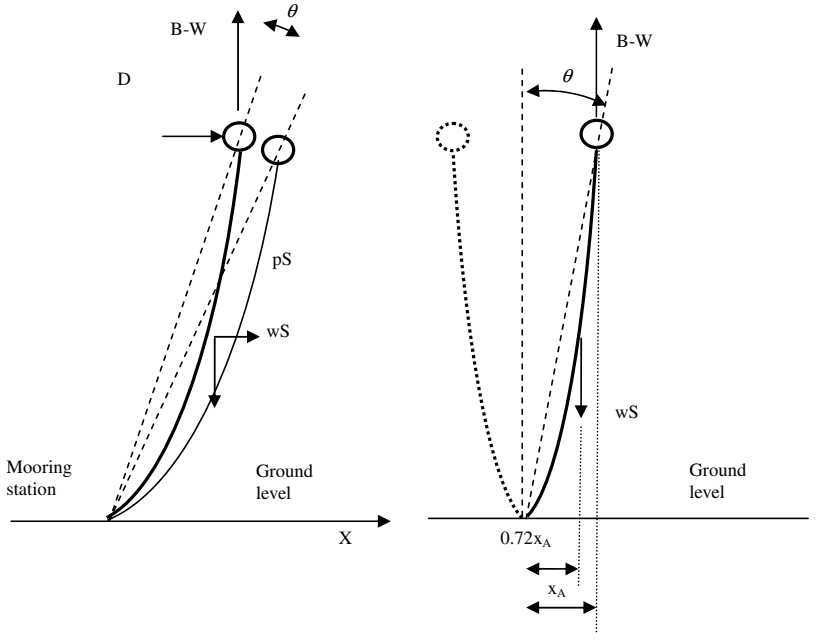

a) **b)**

Fig. 6 Small oscillations of the aerostat with a) wind and b) no wind.

Table 2 Overall resonance frequency verification

Period of oscillations, s	Test 1 sudden 5 m/s gust	Test 2 40 m/s wind plus 5 m/s gust
FE model	168	117
Theory: Eq. (16)	148.8	115.9
Theory: Eq (23) corrected for cable sag	168	——
FE model with high bending stiffness cable	149	——

1. Overall Natural Frequency

Following the simplifications discussed previously, two cases have been tested:

The first one has tested the response of the system (from an initial position of equilibrium, no wind, tether vertical) struck by a horizontal gust with a maximum velocity of 5 m/s and a duration of 130 s.

The second test has considered the response to a gust in the Z direction (out of plane in Fig. 6a, maximum gust velocity 5 m/s, gust duration 10 s) when the system was already subjected to a uniform wind speed of 40 m/s in the X direction. In this case, the model gives an overdamped response, and to force an oscillatory behavior, the damping force has been set to zero. These two conditions represent the two relatively extreme situations, no wind and strong wind, and the period of the oscillations for the two cases are reported in Table 2.

Using Eq. (16), the periods of the oscillation in the two tests are 148.8 and 115.9 s, respectively. Using the model described in this paper, retrieving the period of the oscillations from the time-domain responses shown in Figs. 7 and 8 (showing the displacement of the Aerostat's node together with that of three other nodes positioned at one-fourth, one-half, and three-fourths of the tether line length, respectively), the periods of the oscillations are 168 and 117, respectively. The difference in the period for the first test can be explained by the approximation of the tether as a straight line. In Eqs. (15) and (16), this assumption affects the terms representing the tether's distributed loading, w_t and p, that is applied at the center of the tether. This assumption is justified in the second test case, in which these terms are small compared with the others, and the periods (Table 2, test 2) agree very well. However, in the first test case (no wind) Eq. (16) becomes

$$T = 2\pi\sqrt{\frac{(M_{\text{aero}}S^2 + (m_t S^2/3))}{(B - M_{\text{aero}}g - (w_t S/2))S}} \tag{17}$$

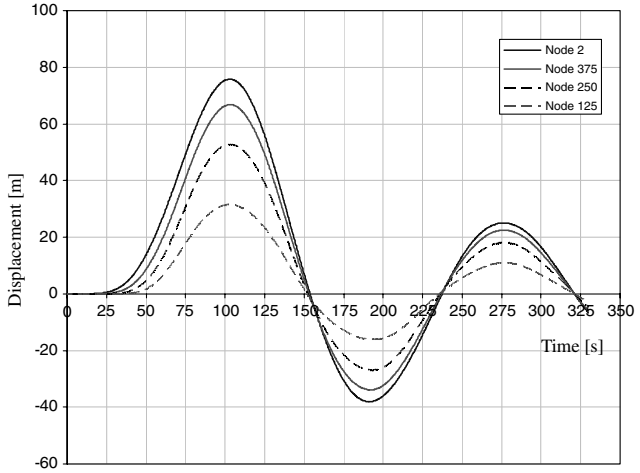

Fig. 7 Response of aerostat and tether line nodes suddenly struck by a horizontal gust (5 m/s, gust duration 130 s) perpendicular to the wind direction.

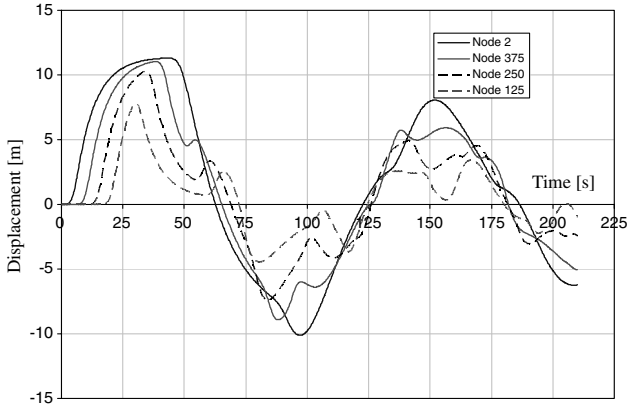

Fig. 8 Out-of-plane response of aerostat and tether line nodes in constant wind (40 m/s) and suddenly struck by a horizontal gust (5 m/s, gust duration 10 s) perpendicular to the wind direction.

and is therefore much more sensitive to the sagging of the tether and, mathematically speaking, to the point of application of the force $w_t S$. In particular, from the response shown in Fig. 7, it appears that the horizontal position of the center of the tether is at 72% of the horizontal position of the aerostat (and not 50% as in the straight line assumption). The sketch in Fig. 6b clarifies this concept. Using the reciprocal of this value (i.e., 1.39) instead of 2 in Eq. (17) gives a period of 168 s, which is in very good agreement with the 170 s calculated from the time-domain response.

To confirm that the reason for the mismatch was indeed the sagging of the tether, a simulation was carried out that artificially increased the modulus of elasticity of the tether to produce enough bending stiffness to maintain the cable straight during the oscillations. In this case, the period of oscillation from the time-domain response was 149 s (see Table 2), in excellent agreement with the original result from Eq. (16).

A point worth noting is the presence of harmonics, visible in Fig. 8, superimposed on the rigid-body behavior. These are produced by the more impulsive nature of the exciting gust compared with the response in Fig. 7. In this case, the oscillations still have periods of seconds, and therefore a 0.1 s time step that was used in the solution procedure is considered appropriate.

2. Critical Damping

Finally, the wind velocity that produces the transition between oscillatory response and asymptotic behavior in this model can be found by including damping in Eq. (15). The aerodynamic damping can be added by including the terms that represent the fluctuation of the aerodynamic forces as a function of the angular velocity $\dot{\theta}$. As will be shown later, the transition occurs for a relatively small wind velocity, which means that the cable is still relatively close to the vertical, and therefore the relative velocity (i.e., the difference between wind speed **v** and the structural velocity vector) is simply $v - \dot{\theta}S$. This is true, as the cosine of the angle between the two vectors is practically 1. Therefore, the moment produced by the aerodynamic forces is

$$\frac{1}{2}\rho_N(v + S\dot{\theta})^2 C_{DS}\pi\left(\frac{\phi_A}{4}\right)^2 S + \frac{\frac{1}{2}\rho_{\text{average}}(v + S\dot{\theta}/2)^2 C_{D\alpha}\phi_T S}{2} \tag{18}$$

Expanding Eq. (18), it is seen that the terms in v^2 are already considered in the stiffness term of Eq. (15), and neglecting the term in $\dot{\theta}^2$ as infinitesimal of higher order yields a damping force equal to

$$\left(\frac{1}{2}\rho_N(2vS)C_{DS}\pi\left(\frac{\phi_A}{4}\right)^2 S + \frac{\rho_{\text{average}}(vS)^2 C_{D\alpha}\phi_T S}{4}\right)\dot{\theta} \tag{19}$$

that can be simply added to Eq. (15). Once the substitution has been carried out, it is possible to set the discriminant of the resulting

second-order equation to zero (corresponding to critical damping) and solve using the velocity as unknown. This delivers a velocity of 5.3 m/s, consistent with the results from the time-domain responses that show oscillatory behavior for wind velocities up to approximately 6 m/s.

It is acknowledged that the model verification carried out does not cover the full range of responses, due to its simplifications. However, the dynamic checks carried out previously, combined with the static tests on the deformed shape of the tether described in the preceding section, give a good indication that the model presented here follows the desired behavior.

IV. Simulations

A. Input Loading

For input loading, gusts with a magnitude profile similar to that shown in Fig. 3, coming from various directions, have been considered. This represents the 66 ft/s gust that is typically considered as the maximum gust load for aircraft structural design purposes and is consistent with the shape of the discrete gust models (see MIL-F-8785 [26]). The duration of the gust is then tuned to produce the maximum excitation of the first mode of vibration (that is, the one that should produce the largest contribution to the aerostat displacement). Here, the system is highly nonlinear and, as discussed in the previous section, there will be conditions in which no oscillation occurs (overdamped situations). In these cases, the highest response would be produced by a gust lasting long enough that the static response would coincide with the dynamic response. A gust of such duration is quite unrealistic, and therefore 2.5 min has been considered as a reasonably conservative estimate (see, for example, [27]) of a gust duration in this case.

The gust velocity vector is summed to a wind vector, which represents a constant wind velocity present up to the moment at which the gust strikes the aerostat and/or the tether, so that the total wind is the sum of the two.

The results shown in this paper are for a gust applied only to the aerostat. However, it is possible to apply any time- and space-variable wind profile along the length of the tether as well.

B. Gust in Line with Wind Direction

In this section, the case of the aerostat in a 20 m/s wind flow and struck by a 20 m/s gust with the same direction (i.e., total maximum wind velocity 40 m/s) is considered.

As discussed in Secs. III.B and IV.A, this system is overdamped, and therefore a 150 s duration (2.5 min) gust was considered. The maximum displacements that occurred along the tether line are shown in Fig. 5, and comparing this curve with that corresponding to the steady-state situation of a 40 m/s wind, it is possible to see that the dynamic response is considerably smaller than the steady-state response. In Fig. 3, it can also be seen that the relative wind velocity is always noticeably smaller than the maximum wind flow velocity.

The rotation of the aerostat is plotted in Fig. 9, in which it is possible to note the overdamped nature of the response and a maximum angle of 7.6 deg, and the response here is also considerably smaller than the angle for the steady-state situation. This rotation is actually caused by the fact that the aerostat is constrained underneath by the tether (and not at the aerostat aerodynamic center of pressure); therefore, when the transient aerodynamic force produced by the gust is applied (at the center of pressure), the temporary misalignment between the aerodynamic force vector and constraint reaction (at the tether attachment) produces a moment and hence a transient rotation of the balloon until a new position of equilibrium is reached. In practice, the rotations in Fig. 9 correspond to the absolute value of the change in slope of the tether at the attachment with the aerostat. If no constraint was present, the aerostat would simply translate (without rotating) pushed by the wind.

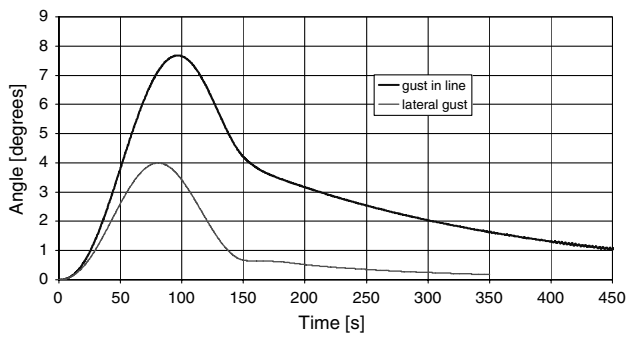

Fig. 9 Rotation of the aerostat produced by a 20 m/s (150 s) gust summed to a 20 m/s wind.

Table 3 Forces at the attachment between the tether and balloon

Response calculation procedure	20 m/s wind and 20 m/s in line gust	20 m/s and 20 m/s lateral gust
Initial condition	427 kt	
Dynamic model	472 kN	433 kN
Quasi-static solution	570 kN	445 kN

Finally, as for the other parameters, the forces at the attachment between the tether and the balloon (Table 3) are considerably smaller than those produced by the steady-state response.

The other case considered here is that of a gust in opposite direction to the wind, and the maximum displacements of the tether in this case are also plotted in Fig. 5. The rotation of the aerostat is actually smaller than that obtained in the previous case, and as the gust actually reduces the wind velocity in this case, the force on the tether will also be smaller than that before the gust struck.

C. Lateral Gust

In this section, the response of the system to a 20 m/s gust applied in a horizontal direction, transverse to the 20 m/s wind flow, is considered. As before, the gust duration is set at 150 s to produce considerable displacements. The response to the gust is shown in Figs. 10 and 11.

Although the response displacement is mainly along the direction perpendicular to the initial wind direction, the tether has the effect of coupling the displacements from the other two directions, such that the resulting displacement of the aerostat is in effect along the three axes simultaneously. The traces of the aerostat displacements in the horizontal and vertical planes are shown in Fig. 11. The maximum force on the tether is shown in Table 2.

V. Discussion

The results of the simulations reported in the previous section show the importance of carrying out a dynamic analysis to avoid overestimating the response of the system to gusts. Here, all the output parameters considered, displacements, rotations, and forces

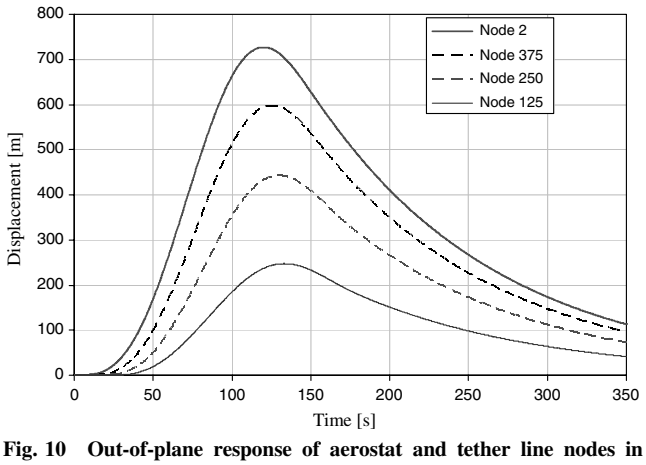

Fig. 10 Out-of-plane response of aerostat and tether line nodes in constant wind (20 m/s) and suddenly struck by a horizontal gust (20 m/s, gust duration 150 s) perpendicular to the wind direction.

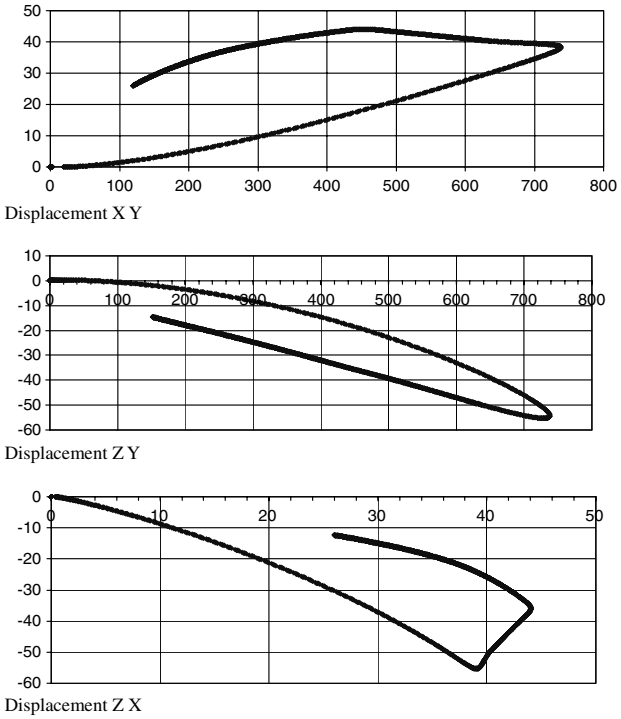

Fig. 11 Trace of the aerostat displacements in the three planes *XY*, *XZ*, and *YZ* for a 20 m/s gust transverse to a 20 m/s wind.

give consistently lower values than the static solutions, and although these results are for a specific case, comparable behaviors should be expected for similar systems. The main reason for this behavior is the high level of damping, and this work has included a good representation of the aerodynamic damping produced by the tether. In reality, other forms of damping (e.g., material damping) will also be present, so that the response should be even more damped than that predicted by the model presented here.

Therefore, it can be concluded that the use of a static model will produce a considerable overestimate of the response. This could be appropriate for an initial stage of the design, but the level of overestimation might not be appropriate for an accurate detailed design.

This model also allows one to calculate the rotations of the balloon resulting from gusts, and that is particularly relevant for applications such as [10], in which a spherical aerostat has to be maintained pointing at the sun.

It must be noted that this procedure dose not explicitly consider vortex-induced vibrations. However, should a description of the loads involved in these phenomena be available as functions of the parameter included in this model (e.g., relative velocity, angles between the tether and wind flow, air density, etc.), then these modes could also be used to reproduce these phenomena. As this paper focused on the system modeling, the complex derivation of the loads involved in vortex-induced vibrations, although a very interesting engineering problem, is deemed to be beyond the scope of the paper.

VI. Conclusions

This paper has illustrated a procedure to calculate the response of a tethered spherical aerostat to gusts including structural nonlinearities and accounting for the fluid–structure interaction of aerostat and tether. In particular, a full 3-D dynamic model of the system was considered, with aerodynamic loads calculated from the relative velocity between a time-varying input airflow and resulting structural velocities.

The static and dynamic responses have been compared with theoretical solutions, and both cases have shown very good agreement of results.

For the specific case examined in this work, the dynamic responses to gusts are considerably smaller than the equivalent steady-state solution, mainly due to the high level of aerodynamic damping in the system. In reality, other forms of damping (e.g., material damping) will be present, so that the response could be even more damped than that predicted by the model presented here.

Therefore, it can be concluded that the use of a static model is likely to produce an overestimate of the response, which could be appropriate for a very early concept study, but that the level of overestimation might not be appropriate for a more accurate preliminary design.

In addition, this model gives the possibility to calculate the rotations of the balloon, which could be relevant for some applications.

Appendix: Derivation of Tether Displacements

From geometrical considerations on the infinitesimal segment of tether shown in Fig. 4, it is possible to write that

$$\mathrm{d}s = \mathrm{d}x\sqrt{1 + (y')^2} \tag{A1}$$

where the slope of the tether line can be calculated from

$$y'(s) = \frac{T_{V0} + \int_0^s w_t\,\mathrm{d}s}{T_{H0} - \int_0^s p\,\mathrm{d}s} \tag{A2}$$

where T_{H0} and T_{V0} are the horizontal and vertical components of the force at the tether mooring station.

Examining Eqs. (11) and (12) it is possible to note that both w_t and p are variable functions of y, as their expressions contain the density, which is a function of the altitude, and the angle between the tether and wind vector (function of y'). Under these conditions, it is not possible to obtain a closed-form solution of the equation describing the tether displacement. However, as the purpose here is to validate the response of the FE model against an exact theoretical result, it is initially possible to simplify the benchmark slightly and perform this validation using constant values for w_t and p (equal to the average of the relevant parameter along the tether line) and then use the same assumption for the FE procedure.

Under these assumptions, the integrals in Eq. (A2) can be easily solved and the solution substituted in Eq. (A1) can be rearranged as

$$\mathrm{d}\,s \Big/ \sqrt{1 + \left(\frac{T_{V0} + w_t s}{T_{H0} - ps}\right)^2} = \mathrm{d}x \tag{A3}$$

Integrating this expression between 0 and s, and simplifying the mathematical notation, calling

$$T_{V0}^2 + T_{H0}^2 = T_0^2 \tag{A4a}$$

$$w_t^2 + p^2 = q^2 \tag{A4b}$$

yields

$$\begin{aligned} x = {} & \left(\frac{T_{H0}}{q} - \frac{2p(T_{V0}w_t - T_{H0}p)}{2q^3}\right) \\ & \times \left(\operatorname{asinh}\left(\frac{q^2 s + (T_{V0}w_t - T_{H0}p)}{\sqrt{q^2T_0^2 - (T_{V0}w_t - T_{H0}p)^2}}\right)\right. \\ & \left. - \operatorname{asinh}\left(\frac{(T_{V0}w_t - T_{H0}p)}{\sqrt{q^2T_0^2 - (T_{V0}w_t - T_{H0}p)^2}}\right)\right) \\ & + \frac{p(\sqrt{(T_{H0} - ps)^2 + (T_{V0} + w_t s)^2} - T_0)}{q^2} \end{aligned} \tag{A5}$$

The stretching of the cable can be included by adding two extra terms to this equation: the first term to represent the horizontal stretching due to the horizontal load produced by the aerostat and the second one to include the contribution due to the horizontal load distributed along the tether:

$$\Delta x = + \frac{T_{H0} s}{EA/L} + \frac{p s^2}{2(EA/L)} \tag{A6}$$

The same procedure can now be applied starting from

$$\mathrm{d}\, s = \mathrm{d}y \sqrt{1 + \left(\frac{1}{y'}\right)^2} \tag{A7}$$

to obtain y as a function of s:

$$\begin{aligned} y = & \left(\frac{T_{V0}}{q} - \frac{2w(T_{V0} w_t - T_{H0} p)}{2q^3}\right) \\ & \times \left(\operatorname{asinh}\left(\frac{w^2 s + (T_{V0} w_t - T_{H0} p)}{\sqrt{q^2 T_0^2 - (T_{V0} w_t - T_{H0} p)^2}}\right)\right. \\ & \left. - \operatorname{asinh}\left(\frac{(T_{V0} w_t - T_{H0} p)}{\sqrt{q^2 T_0^2 - (T_{V0} w_t - T_{H0} p)^2}}\right)\right) \\ & + \frac{w(\sqrt{(T_{H0} - ps)^2 + (T_{V0} + w_t s)^2} - T_0)}{q^2} \end{aligned} \tag{A8}$$

The stretching of the cable can be included here by summing the following terms to the preceding equation:

$$\Delta y = + \frac{T_{V0} s}{EA/L} + \frac{w_t s^2}{2(EA/L)} \phi \tag{A9}$$

Note that when the horizontal load is neglected, Eqs. (A5) and (A8) can be simplified to become the classic catenary equations.

Acknowledgment

The author would like to thank Samuel Roberts for his help.

References

[1] Colozza, A., and Dolce, J. L., "High-Altitude, Long-Endurance Airships for Coastal Surveillance," NASA TM 2005-213427, 2005.

[2] "Tethered Aerostat Radar System" U.S. Air Force, Air Combat Command, Langley AFB, VA, Feb. 2006.

[3] Bely, P., and Ashford, R. L., "High-Altitude Aerostats as Astronomical Platforms," *Proceedings of SPIE: The International Society for Optical Engineering*, Vol. 2478, 1995, pp. 101–116. doi:10.1117/12.210916

[4] Badesha, S. S., "SPARCL: A High-Altitude Tethered Balloon-Based Optical Space-to-Ground Communication System," *Proceedings of SPIE: The International Society for Optical Engineering*, Vol. 4821, 2002, pp. 181–193. doi:10.1117/12.450641

[5] Stanney, K. A., and Rahn, C. D., "Response of a Tethered Aerostat to Simulated Turbulence," *Communications in Nonlinear Science and Numerical Simulation*, Vol. 11, No. 6, 2006, pp. 759–776. doi:10.1016/j.cnsns.2005.01.001

[6] Jones, S. P., "Nonlinear Dynamic Simulation of a Moored Aerostat," *7th AIAA Lighter-Than-Air Technology Conference*, AIAA, New York, 1987, pp. 72–77.

[7] Jones, S. P., and Schroeder, L. D., "Nonlinear Dynamic Simulation of a Tethered Aerostat: A Fidelity Study," *Journal of Aircraft*, Vol. 38, No. 1, 2001, pp. 64–68. doi:10.2514/2.2735

[8] Miller, J. I., and Nahon, M., "Analysis and Design of Robust Helium Aerostats," *Journal of Aircraft*, Vol. 44, No. 5, 2007, pp. 1447–1458. doi:10.2514/1.25627

[9] Badesha, S. S., and Bunn, J. C., "Dynamic Simulation of High-Altitude Tethered Balloon System Subject to Thunderstorm Windfield," AIAA Atmospheric Flight Mechanics Conference and Exhibit, Monterey, CA, AIAA Paper 2002-4614, Aug. 2002.

[10] Aglietti, G. S., Markvart, T., Tatnall, A. R., and Walker, S. J., "Solar Power Generation Using High Altitude Platforms Feasibility and Viability," *Progress in Photovoltaics: Research and Applications*, Vol. 16, No. 4, 2008, pp. 349–359. doi:10.1002/pip.815

[11] Franz, S. Hover, Mark A. Grosenbaugh, and Michael S. Triantafyllou, "Calculation of Dynamic Motions and Tensions in Towed Underwater Cables," *IEEE Journal of Oceanic Engineering*, Vol. 19, No. 3, July 1994, pp. 449–457. doi:10.1109/48.312921

[12] Huang, S., "Dynamic Analysis of Three-Dimensional Marine Cables," *Ocean Engineering*, Vol. 21, No. 6, 1994, pp. 587–605. doi:10.1016/0029-8018(94)90008-6

[13] Grosenbaugh, M. A., "Transient Behavior of Towed Cable Systems During Ship Turning Maneuvers," *Ocean Engineering*, Vol. 34, Nos. 11–12, Aug. 2007, pp. 1532–1542. doi:10.1016/j.oceaneng.2007.01.002

[14] Lunnon, G., "Fluid Resistance to Moving Spheres," *Proceedings of the Royal Society of London A*, Vol. 110, 1926, pp. 302–326. doi:10.1098/rspa.1926.0017

[15] Sakamoto, H., and Haniu, H., "A Study of Vortex Shedding from Spheres in a Uniform Flow," *Journal of Fluids Engineering*, Vol. 112, No. 4, 1990, pp. 386–392. doi:10.1115/1.2909415

[16] Constantinescu, G., and Squires, K., "Numerical Investigations of Flow over a Sphere in the Subcritical and Supercritical Regimes," *Physics of Fluids*, Vol. 16, No. 5, 2004, pp. 1449–1466. doi:10.1063/1.1688325

[17] Howe, M. S., Lauchle, G. C., and Wang, J., "Aerodynamic Lift and Drag Fluctuations of a Sphere," *Journal of Fluid Mechanics*, Vol. 436, 2001, pp. 41–57. doi:10.1017/S0022112001003925

[18] Williamson, C. H. K., and Ovardhan, R. G., "Dynamics and Forcing of a Tethered Sphere in a Fluid Flow," *Journal of Fluids and Structures*, Vol. 11, No. 3, 1997, pp. 293–305. doi:10.1006/jfls.1996.0078

[19] Lee, H., Thompson, M. C. and Hourigan, K., "Vortex-Induced Vibration of a Neutrally Buoyant Tethered Sphere," *Proceedings of the 16th Australasian Fluid Mechanics Conference*, School of Engineering, Univ. of Queensland, Brisbane, QLD, Australia 2–7 Dec. 2007, pp. 580–585.

[20] Williamson, C. H. K., and Govardhan, R., "Vortex-Induced Vibrations," *Annual Review of Fluid Mechanics*, Vol. 36, 2004, pp. 413–455. doi:10.1146/annurev.fluid.36.050802.122128

[21] Govardhan, R. N., and Williamson, C. H. K., "Vortex-Induced Vibrations of a Sphere," *Journal of Fluid Mechanics*, Vol. 531, 2005, pp. 11–47. doi:10.1017/S0022112005003757

[22] Brika, D., and Laneville, A., "Vortex-Induced Vibrations of a Long Flexible Circular Cylinder," *Journal of Fluid Mechanics*, Vol. 250, 1993, pp. 481–508. doi:10.1017/S0022112093001533

[23] Newman, D. J., and Karniadakis, A. E., "A Direct Numerical Simulation Study of Flow Past a Freely Vibrating Cable," *Journal of Fluid Mechanics*, Vol. 344, 1997, pp. 95–136. doi:10.1017/S002211209700582X

[24] "Mean Forces, Pressures and Flow Field Velocities for Circular Cylindrical Structures: Single Cylinder with Two-Dimensional Flow," ESDU International, Data Item 80025, Amendment C, London, 1986.

[25] Khoury, G. A., and Gillett, J. D., *Airship Technology*, Cambridge Aerospace Series, Cambridge Univ. Press, Cambridge, England, U.K., 2004.

[26] "Flying Qualities of Piloted Airplanes," U.S. Dept. of Defense, MIL-SPEC MIL-F-8785, 1980.

[27] Barry, R. G., and Chorley, R. J., *Atmosphere, Weather and Climate*, Routledge, London, 1992.